J Mater Sci: Mater Electron (2022) 33:15222–15231

Solar light performances of *n*-ZnO nanorods/*p*-Si-based photodetectors under high illumination intensity

O. Ozturk[1,*], B. M. Candan[1], S. Kurnaz[2], O. Cicek[1], and A. T. Tasci[1]

[1] *Department of Electrical and Electronics Engineering, Faculty of Engineering and Architecture, Kastamonu University, 37210 Kastamonu, Turkey*

[2] *Central Research Laboratory, Kastamonu University, 37210 Kastamonu, Turkey*

Received: 28 March 2022
Accepted: 16 May 2022
Published online: 6 June 2022

ABSTRACT

We present ZnO nanorod/ZnO thin film structures synthesized at different molarities and growth times using a hydrothermal method, exhibiting uniquely solar sensing characteristics. ZnO thin film was deposited on *p*-Si(100) substrate by using RF sputter. ZnO nanorods with different molarities (10 and 20 mM) and growth times (2, 3, and 4 h) were fabricated at 90 °C by using the hydrothermal method on the *n*-ZnO/*p*-Si. The surface texture was also examined by scanning electron microscopy. The diameter of ZnO NRs was in the range of 62–119 nm. The current–time measurements were done under solar light illumination intensity (50 and 100 mW/cm^2) and forward bias voltage (1, 5, and 10 V). Decay time (τ_d), rise time (τ_r), detectivity (D^*), responsivity (R), and sensitivity (S) parameters were calculated. Samples produced at 2 h and 3 h in 10 mM solution performed best due to low τ_d, τ_r, and high D^*, R, S. Especially, the S for the PD_{102} changed from 4.24 to 11.8, while it was in the range of 0.41–7.33 for the PD_{103}. The R was 5.81 AW^{-1} in PD_{102} and 1.19 AW^{-1} in PD_{103}. The D^* was 10^9–10^{11} cmHz$^{1/2}$/W in PD_{102} and 10^{10}–10^{11} cmHz$^{1/2}$/W in PD_{103} at ± 6 V.

1 Introduction

Zinc oxide (ZnO) is the most attractive semiconductor for electronic applications, because of its large bandgap energy of 3.37 eV, high exciton binding energy with 60 meV, electrical conductivity, and optical transparency. ZnO can be grown as different kinds of one-dimensional (1D) nanostructures such as nanocombs, nanorods (NRs), nanobelts, nanoflowers, and nanopillars. These ZnO nanostructures have various applications such as transistor, gas sensor, spintronic, solar cell, photodiode, and UV photodetector applications [1–3]. Many efforts have been made on 1D ZnO which improves the photodetection and photoresponse behaviors. It is known that photodetection and photoresponse of the ZnO NRs depend on the surface condition, structural quality, methods of synthesis, and rate of oxygen adsorption and photodesorption. Therefore, it is expected that arrays of NRs, surface modification, or

Address correspondence to E-mail: oozturk@kastamonu.edu.tr

https://doi.org/10.1007/s10854-022-08440-1

structural improvement can enhance the photosensitivity as well as photoresponse [4]. ZnO NRs with controlled shape and order could be grown by thermal evaporation [5], chemical vapor deposition [6], radio frequency (RF) sputtering [7], hydrothermal methods [8], etc. Among these methods, ZnO NRs grown by the hydrothermal method has been regarded as a source of *n*-type conductive semiconductor due to native point defects such as zinc interstitials and oxygen deficiencies [9]. Since high quality and stable *p*-type doping has been a problem for a long time, developing a reliable *p*–*n* ZnO-based homojunction device has remained a challenge [10]. To solve this problem, an alternative approach is to utilize *p*-type substrates such as *p*-Si.

n-ZnO/*p*-Si heterojunction-based devices are potential candidates for UV and visible light detection which detect UV photons in the depleted *n*-ZnO and visible photons in the depleted *p*-Si [11]; however, these photodetectors (PDs) typically have low responsivity, due to the energy barrier at the junction interface. Several studies have used *n*-ZnO/*p*-Si heterojunctions for UV and visible light applications [2]. The PDs are light-sensitive devices used to detect optical signals through electronic processes. The electrical behavior involves three steps: (1) carrier generation by absorption of the incident light, of which the photon energy is higher than the bandgap of device materials; (2) carrier transport; and (3) interaction of the current with the external circuit to provide the output signal [12].

In the present work, we investigated the photodetector properties of ZnO NR-based PDs. ZnO NRs with different molarities (10 and 20 mM) and growth times (2, 3, and 4 h) were fabricated on *n*-ZnO/*p*-Si substrate using the hydrothermal method. By applying solar light illumination intensity (50 and 100 mW/cm^2) and forward bias voltage (1, 5, and 10 V), the photodetector properties such as decay time (τ_d), rise time (τ_r), detectivity (D^*), responsivity (R), and sensitivity (S) parameters were investigated.

2 Experimental procedure

ZnO seed layers with 100 nm thicknesses were deposited on *p*-Si(100) substrates which had resistivity of a 1–10 Ω cm using RF sputter (NVTS 400, Nanovak). Before RF sputtering process, the substrates were immersed in HF + 20H_2O solution and allowed to stand for 30 s which was used to remove native oxides and quenched in deionized (DI) water. Then, the substrates were cleaned ultrasonically with ethanol and DI water. The RF sputter was carried out at 50 °C using a ZnO target. The pressure of Ar:O_2 (80:20) gas was 10 mTorr. RF power output was fixed at 100 W. The base vacuum pressure of the sputtering system was 1×10^{-6} Torr. After deposition, the samples were immediately annealed at 600 °C in air ambient for 30 min.

ZnO NRs were grown on the ZnO seed layer by using a hydrothermal method. The ZnO/*p*-Si substrates were placed in 30 ml growth solution of DI water with zinc acetate dihydrate ($Zn(CH_3COO)_2$-$2H_2O$) and hexamethylenetetramine ($C_6H_{12}N_4$) in equimolar molar concentrations (10 and 20 mM). The autoclave was kept in an oven at 90 °C for 2 h, 3 h, and 4 h. After the reaction, the samples were washed with DI water to remove residual salts and organic materials. Then, they were dried in an oven at 90 °C.

100 nm aluminum (Al) metal as an ohmic contact was deposited by DC sputter (NVTS 400, Nanovak) on the backside of *p*-Si substrate. The as-grown metal contacts were annealed at 450 °C for 20 min. Then, 100 nm Al Schottky or rectifier contacts were deposited by using DC sputter and their shapes were circular dots with a diameter of 2 mm. DC power output was fixed at 135 W and the deposition chamber was evacuated to the pressure of 40 mTorr under Ar gas. The classification of the samples was made according to their molarities (10 and 20 mM) and growth times (2, 3, and 4 h). It was referred to as PD_{102}, PD_{103}, PD_{104}, PD_{202}, PD_{203}, and PD_{204} PDs.

The nanorod dimension and orientation were evaluated by scanning electron microscope (SEM; FEI Quanta FEG 250). The current–time ($I(t)$) measurements dependent on solar light illumination intensity (50 and 100 mW/cm^2) and forward bias voltage (1, 5, and 10 V) were performed by the use of Keithley 2400 source meter and solar simulator (Scientech SF300A). The wavelength of the 300 W Xenon lamp of the solar simulator ranged from 300 to 2000 nm which was used for photocurrent measurement. The solar light was dropped by a mechanical chopper at a frequency of 1.62 Hz. A schematic illustration of the fabricated ZnO NR-based PD with forward-biased measurement, energy band diagram, and carrier transport of forward-biased PD under solar light illumination is presented in Fig. 1a and b.

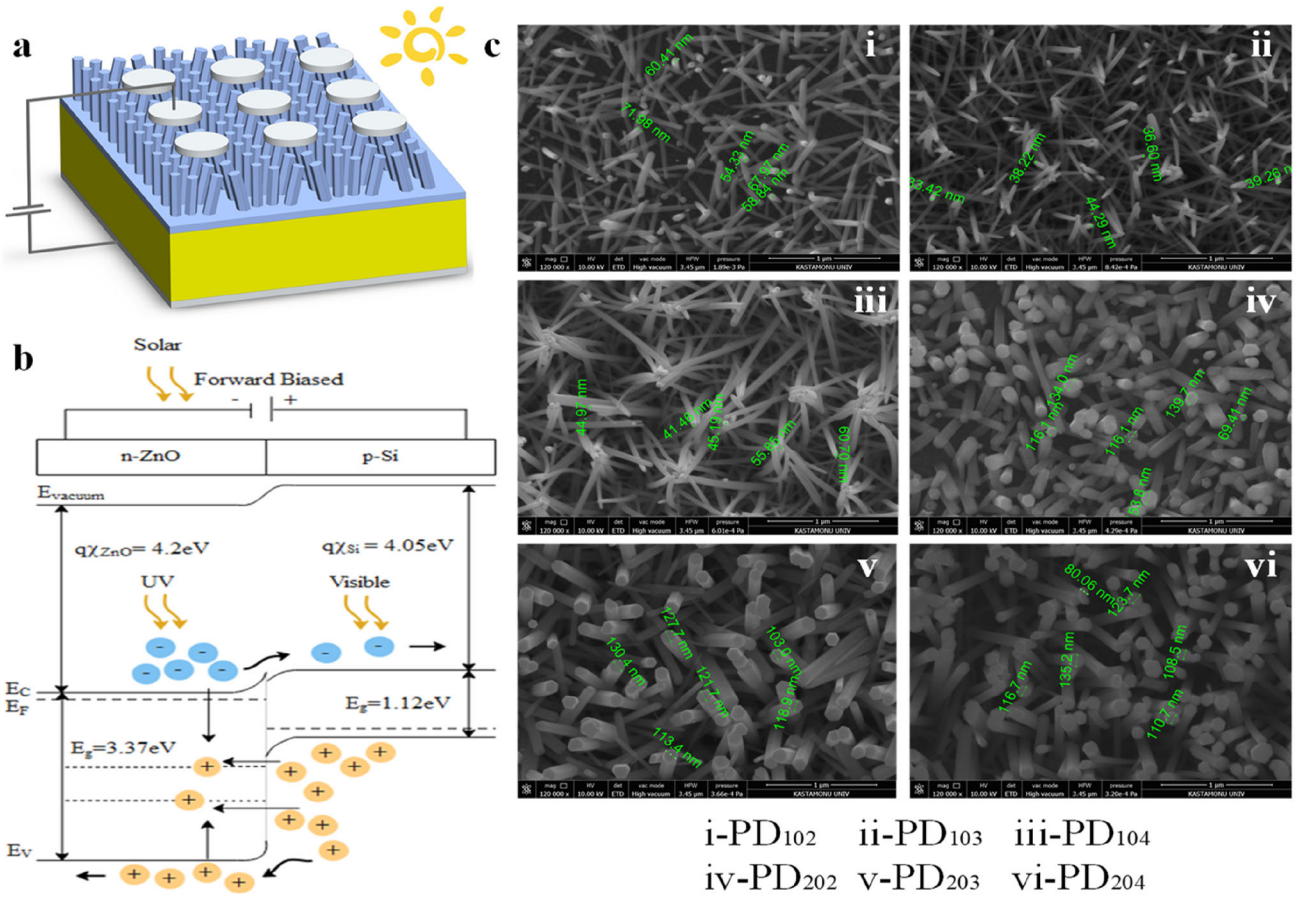

Fig. 1 **a** Schematic illustration of the *n*-ZnO/*p*-Si PD fabricated, **b** energy band diagram and carrier transport of forward-biased PD under solar light illumination, **c** SEM images (top) of (i) PD_{102}, (ii) PD_{103}, (iii) PD_{104}, (iv) PD_{202}, (v) PD_{203}, and (vi) PD_{204} PDs

3 Results and discussion

Figure 1c shows the top view SEM images of PD_{102}, PD_{103}, PD_{104}, PD_{202}, PD_{203}, and PD_{204} PDs, respectively. It can be seen from the images that ZnO NRs vertically oriented on the ZnO seed layer/*p*-Si. The average diameter of ZnO NRs was measured to be 62 nm, 39 nm, 38 nm, 121 nm, 119 nm, and 118 nm, respectively. It is seen that the diameters of ZnO NRs increase 2–3 times as the molarity increases. As seen in Fig. 1c, ZnO NRs appear to tilt as well as grow vertically. Some factors cause this situation. Firstly, each crystalline surface of the seed layer grains acts as nuclei for the growth of NRs [10]. The orientation of the *p*-Si substrate is in the (001). Even though the ZnO seed layer deposited on *p*-Si substrate is in the (002) orientation, the orientation of the ZnO is distorted with the annealing process and the (100) orientation of the *p*-Si. Therefore, large lattice misfits between ZnO NRs and *p*-Si substrate deteriorate the quality of the NRs [12–14]. Secondly, it is affected by the positioning angle of the *n*-ZnO/*p*-Si substrate in the hydrothermal autoclave reactor. Finally, some factors such as the precursor concentration, growth time, seed layer thickness, pH of the growth solution, and growth temperature affect the quality of ZnO NRs [15]. Considering all these factors, it seems that ZnO NRs are tilted.

The ZnO is an *n*-type semiconductor and the conductivity of ZnO NRs depends mainly on the oxygen (O_2) amount that plays a crucial role in the photoresponse of ZnO [15]. It is known that the photoresponse of the ZnO NRs consists of two parts: a rapid process of photogeneration and recombination of electron–hole (e^-–h^+) pairs, and a slow process of surface adsorption and photodesorption of oxygen molecules [4]. In dark conditions, oxygen molecules tend to be desorbed on ZnO surface by capturing free electrons from the NRs according to $O_2(g) + e^- \rightarrow O_2^-(abs)$ where O_2 is the oxygen molecule, e^- is

the free electron, and O_2^- is the adsorbed oxygen ion on the surface of ZnO. The adsorbed oxygen ions form a barrier near the surface due to the bending of the conduction band and the valence band. The formation of a large number of ionized oxygen on the NRs surface enhances the band bending, resulting in a very low conductivity before illumination [4, 16].

When the PDs are illuminated with solar light, e^-–h^+ pairs are generated when the energy of solar light is greater than the E_g of ZnO NRs/ZnO seed layer (~ 3.37 eV or ~ 370 nm). Furthermore, a visible light arriving at the junction will pass through the ZnO layer as a transparent window and be absorbed in the underlying *p*-Si (1.12 eV or ~ 1107 nm) to generate e^-–h^+ pairs [17–19]. The e^-–h^+ pairs are separated by a local electric field in the depletion region. This electric field pushes the holes toward the surface of the NRs and recombines with electrons from the adsorbed oxygen ions. This condition in turn causes releasing oxygen atoms from NRs surface which neutralize the oxygen ions by the reaction of O_2^{-} (ads) + $h^+ \rightarrow O_2$(g). At the same time, the photogenerated electrons fill the conduction band and contribute to photoconduction. Therefore, an increase in electrons concentration leads to an increase in conductivity. Consequently, the observed high photocurrent can be attributed to light-induced charge carrier generation at the depletion region of the NRs [20]. When the solar light is switched off, oxygen once again begins to be adsorbed on the surface, thereby decreasing the conductivity of the PD [16].

The *S*, *R*, *D**, τ_r, and τ_d are important parameters which are assessed the performance of the fabricated PDs. *S* is the ratio of photocurrent (I_{ph}) to dark current which is defined in Eq. 1 [16]. *R* is defined as the ratio of the photocurrent (I_{ph}) to the optical power (P_{opt}) incident on the active area of the PDs device in Eq. 2 [15]. *D** is another parameter that represents the detector's ability to measure signals concerning its noise level [21]. *D** is calculated from the dark current and responsivity using the expression in Eq. 3 [22].

$$S = \frac{I_{ph} - I_{drk}}{I_{drk}} \tag{1}$$

$$R = \frac{I_{ph}}{P_{opt}A} \tag{2}$$

$$D^* = \frac{A^{1/2}R}{\sqrt{2eI_{drk}}} \tag{3}$$

The τ_r defines the time required for photocurrent to increase from %10 to 90% of its maximum rise value in Eq. 4, while τ_d is the time needed to reach 10% from 90% of the maximum rise in Eq. 5 [16, 23].

$$\tau_r = \tau_{\%90} - \tau_{\%10} \tag{4}$$

$$\tau_d = \tau_{\%10} - \tau_{\%90} \tag{5}$$

I(*t*) measurements obtained under forward-biased of 1 V, 5 V, and 10 V and illumination intensity of 50 mW/cm^2 and 100 mW/mm^2 are given in Fig. 2. The current passing through the Schottky barrier can be described as follows:

$$I = I_o\left[\exp\left(\frac{q(V - IR_s)}{nkT}\right)\right] \tag{6}$$

In Eq. 6, *n* is the ideality factor, *q* is the charge of electron equal to 1.602 × 10^{-19} C, *V* is the applied bias voltage, IR_s is caused by the voltage drop on the series resistance (R_s) on the structure. This drop across a rectifying contact is equal to the difference between the total potential and the voltage on the R_s when $V > 3kT/q$. *k* is the Boltzmann's constant equals to approximately 1.3807 × 10^{-23} J/K [1]. Solar light dropped on the PD with an average frequency of 1.62 Hz, and the photocurrent (I_{ph}) suddenly increased with the opening of the light and reached saturation. The photocurrent is expressed as

$$I_{ph} = Aq\left(\Delta n_{ph}\upsilon_n - \Delta p_{ph}\upsilon_p\right) \tag{7}$$

where Δn_{ph} and Δp_{ph} are the average electron and hole density generated by the solar light; and υ_n and v_ρ are the average velocities of electrons and holes. Because the electric field strength inside the depletion region increases as the bias voltage increases, electrons and holes will have higher average velocities. As a result, the photocurrent increases with increased bias voltage [12]. When the solar light is turned off, the current reaches its initial value. It has been observed to increase the amount of photocurrent generated with increasing illumination intensity. The τ_r, τ_d, *S*, and *R* parameters of the fabricated PDs calculated from the *I*(*t*) measurements in Fig. 2 are included in Table 1.

As seen in Table 1, when 1 V was applied to the PD_{102}, the τ_r was 70 ms and 77 ms under 50 and 100 mW/cm^2, while the τ_r was 76 ms and 68 ms at 10 V. The τ_d was 78 ms and 88 ms at 1 V, while it was 65 ms and 81 ms at 10 V. Although the *S* reached the highest value of 10 and 11.8 at 5 V, it decreased at

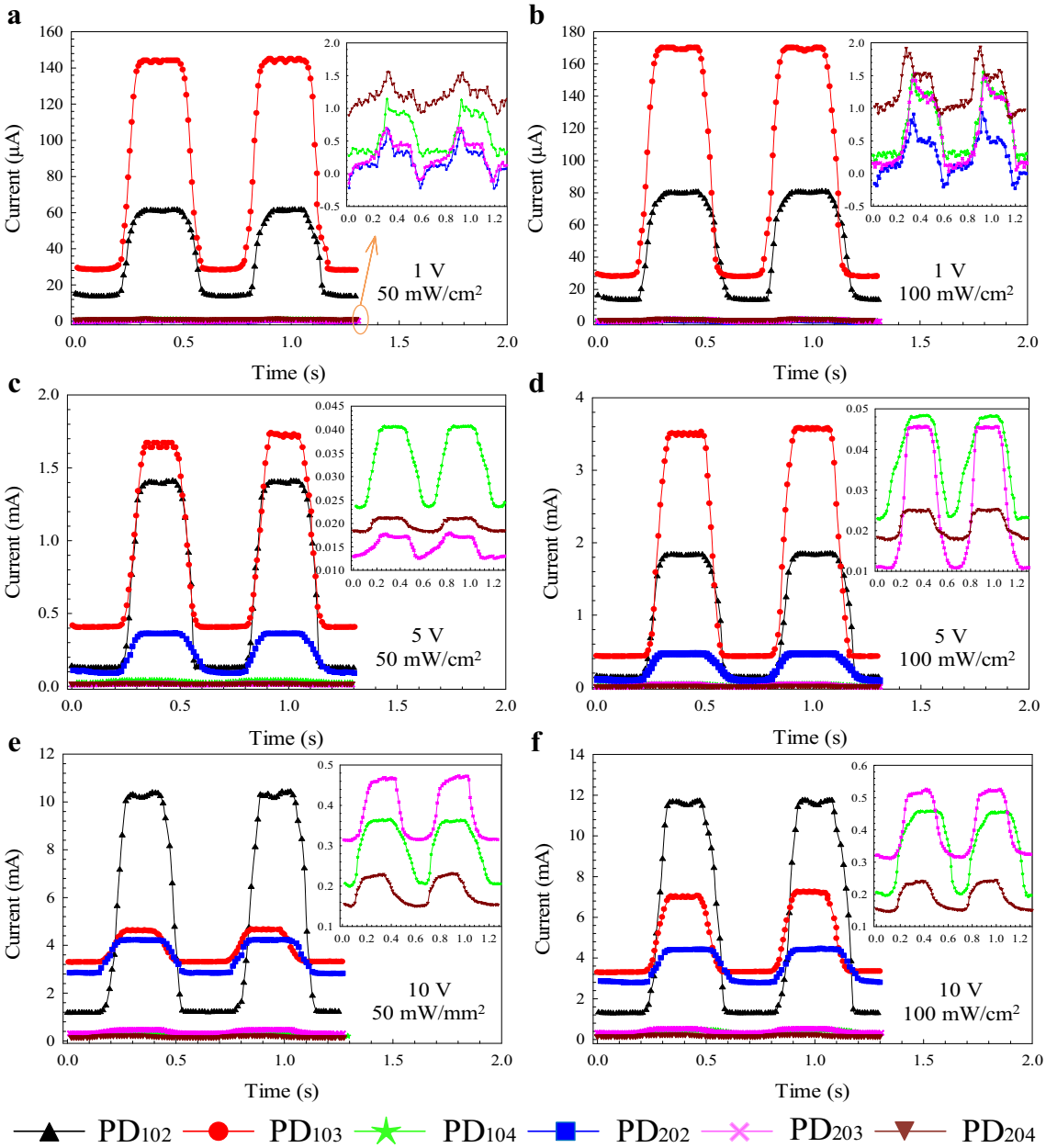

Fig. 2 The $I(t)$ measurements of **a** 1 V and 50 mW/cm^2, **b** 1 V and 100 mW/cm^2, **c** 5 V and 50 mW/cm^2, **d** 5 V and 100 mW/cm^2, **e** 10 V and 50 mW/cm^2, and **f** 10 V and 100 mW/cm^2

10 V. The R reached 5.81 AW^{-1} and 3.31 AW^{-1} with increasing illumination intensity and bias voltage.

As observed in Table 1, when 1 V was applied to the PD_{103}, the τ_r was 69.3 ms and 72 ms under 50 and 100 mW/cm^2, While it was 79.6 ms and 66.7 ms at 10 V. The τ_d increased as the bias voltage rises. The τ_d increased with the rise of the voltage, from 68.6 ms and 63 ms at 1 V to 75 ms and 77 ms at 10 V. Although the S increased under 50 mW/cm^2 and 100 mW/cm^2, it decreased with increasing voltage. On the other hand, although the R increased with the bias voltage under 100 mW/cm^2, it had approximately the same values at 5 V and 10 V under 50 mW/cm^2.

Although 1 V was applied to the PD_{104}, a photocurrent reaching the saturation point could not be observed. So the τ_r, τ_d, S, and R values could not be calculated and are shown in Fig. 2a and b. Looking at Table 1, the photoresponse properties were calculated according to 5 V and 10 V. At 50 mW/cm^2, the

Table 1 Photoresponse properties of ZnO NR-based PDs

Name	Intensity of light (mW/cm^2)	Bias (V)	Rise time (ms)	Decay time (ms)	Sensitivity	Responsivity (A/W)
PD_{102}	50	1	70 ± 5.1	78 ± 2.0	4.21	0.03
		5	58 ± 3.6	60 ± 5.4	10	0.81
		10	76 ± 1.8	65 ± 2.8	7.73	5.81
	100	1	77 ± 1.3	88 ± 4.6	4.92	0.02
		5	60 ± 5.3	64 ± 2.9	11.8	0.54
		10	68 ± 5.8	81 ± 9.4	8	3.31
PD_{103}	50	1	69.3 ± 6	68.6 ± 1.3	4.05	0.07
		5	69 ± 5.4	67 ± 6.5	3.12	0.80
		10	79.6 ± 5	75 ± 2.8	0.41	0.85
	100	1	72 ± 1.1	63 ± 3.5	4.71	0.04
		5	68 ± 1.2	65 ± 2.8	7.33	1.00
		10	66.7 ± 4	77 ± 3.5	1.20	1.19
PD_{104}	50	1*	–	–	–	–
		5	112 ± 1	133 ± 3.0	1.04	0.01
		10	97 ± 5.4	166 ± 3.0	1.16	0.1
	100	1*	–	–	–	–
		5	160 ± 5	107 ± 3.5	1.12	0.008
		10	156 ± 6	97 ± 0.3	1.28	0.08
PD_{202}	50	1*	–	–	–	–
		5	73 ± 1.7	97.3 ± 1.5	3.05	0.17
		10	72.6 ± 1.4	82.3 ± 2.3	0.48	0.86
	100	1*	–	–	–	–
		5	72.3 ± 1.8	105 ± 2.9	4.10	0.12
		10	79 ± 2.0	85 ± 2.8	0.55	0.52
PD_{203}	50	1*	–	–	–	–
		5	219 ± 4.6	65 ± 8.6	0.41	0.003
		10	114 ± 3.3	82 ± 4.1	0.51	0.1
	100	1*	–	–	–	–
		5	85.3 ± 3.1	116 ± 4.0	0.74	0.01
		10	85.6 ± 8.2	106.6 ± 3.0	0.47	0.06
PD_{204}	50	1*	–	–	–	–
		5	65.3 ± 7.6	175 ± 9.7	0.27	0.004
		10	113 ± 6.2	180 ± 10.0	0.52	0.05
	100	1*	–	–	–	–
		5	83 ± 11.0	170 ± 5.8	0.15	0.001
		10	92 ± 5.0	173 ± 6.5	0.61	0.03

*Not saturated level

τ_r decreased from 112 to 97 ms with bias voltage increase, while at 100 mW/cm^2, it was almost the same. With the increase in illumination intensity at 5 V, the τ_d decreased from 133 to 107 ms at 5 V and from 166 to 97 ms at 10 V.

The photoresponse properties of the $I(t)$ measurements of PD_{202}, PD_{203}, and PD_{204} are given in Table 1. It was seen that the $I(t)$ measurements at 1 V could not reach saturation. When 5 V and 10 V were applied to the PD_{202}, it was seen that it reached saturation level. As seen in Table 1, it was 73 ms and 72 ms at 50 mW/cm^2, while it was 72.3 ms and 79 ms at 100 mW/cm^2. Especially at 5 V, while the τ_r did not change, it increased slightly at 10 V. It was observed that τ_d decreased with the increase of bias voltage and illumination intensity. The S decreased from 3.05 to 0.48 under 50 mW/cm^2. Under 100 mW/cm^2, it decreased from 4.1 to 0.55.

As observed in Table 1, with the increase of the bias voltage of the PD_{203}, the τ_r decreased from 219 to 114 ms under 50 mW/cm^2. Under 100 mW/cm^2, it was 85.3 ms and 85.6 ms which were very close to

each other. While the τ_d increased from 65 to 82 ms under 50 mW/mm^2, it decreased from 116 to 106.6 ms under 100 mW/cm^2. The S increased from 0.41 to 0.51 under 50 mW/cm^2. It decreased from 0.74 to 0.47 under 100 mW/cm^2. The R appeared to increase with increasing light intensity and bias voltage.

As illustrated in Table 1, the τ_r increased from 65.3 to 113 ms with the increase in bias voltage of PD_{204}, under 50 mW/cm^2. Under 100 mW/cm^2, it increased from 83 to 92 ms. The τ_d increased from 175 to 180 ms under 50 mW/mm^2, while it increased from 170 to 173 ms under 100 mW/cm^2. The S increased from 0.27 to 0.52 under 50 mW/mm^2. Under 100 mW/cm^2, the S increased from 0.15 to 0.61. It was observed that the R increased to 0.05 AW^{-1} and 0.03 AW^{-1} with increasing illumination intensity and bias voltage.

Figure 2 shows a small fraction of the $I(t)$ measurements. It is seen that as the time increased, the dark current value increased. The photocurrent had also increased at the same rate. Considering the reason, the PD heated up at high solar illumination intensity (50 and 100 mW/cm^2). Due to the non-centrosymmetric crystal structure and specific polar axis along the direction of spontaneous polarization, ZnO is a common pyroelectric material that shows a pyroelectric effect. When lights radiate to the surface of ZnO, the light-heating effect will instantaneously produce a temperature variation in the material, thereby generating pyroelectric polarization charges on the surface of ZnO and these charges contribute to the photocurrent measurement. Moreover, the light-heating effect is decreasing gradually with the wavelength decreasing to the visible range, even to UV waves [24]. In our measurement system, the wavelength of the 300 W Xenon lamp of the solar simulator ranges from 300 to 2000 nm. Since the infrared region is also included between 750 and 2000 nm, the light-heating effect affects the photocurrent measurements.

For PD_{104}, PD_{202}, PD_{203}, and PD_{204}, it was seen that the $I(t)$ measurements at 1 V did not reach saturation level which was affected by some factors. Firstly, the bandgap and electron affinity values of ZnO and p-Si are $E_{g,ZnO}$ = 3.37 eV, χ_{ZnO} = 4.35 eV, $E_{g,Si}$ = 1.12 eV, χ_{Si} = 4.05 eV, respectively, in Fig. 1b. Considering energy bandgap of n-ZnO/p-Si heterojunction, a barrier is formed in the conductivity band offset ($\Delta E_c = \chi_{ZnO} - \chi_{Si}$) 0.3 eV and valence band offset ($\Delta E_v = E_{g,ZnO} - E_{g,Si}$) 2.55 eV [25]. The visible light generated e^-–h^+ in p-Si drift toward the Al electrodes side owing to the forward bias. As the forward bias voltage increases, photogenerated e^-–h^+ of p-Si surpass the conductivity/valance band offset and contribute to the photocurrent. Secondly, the ZnO seed layer was coated on p-Si(100) substrate using the RF sputtering method that formed a thin SiO_2 layer between p-Si and ZnO layer. This barrier results in a low response for visible light detection [26, 27]. Thirdly, the size of metal electrodes can strongly affect the distribution of the electric field built in the Schottky junction. As it is well known, the electric field can prevent the recombination of photogenerated e^-–h^+ pairs, and efficiently separate the photogenerated carriers [28]. Lastly, the high crystal quality of the nanostructures leads to the reduction of the density of charge-trap centers as a result of defects in the crystalline structure of nanostructures, therefore significantly improving the photoresponse. The defects have a strongly negative effect on the photoresponse [29]. In Fig. 2a and b, a sudden increase in photocurrent was observed under solar light illumination intensity. Because the weakly adsorbed atmospheric oxygen molecules are desorbed, thereby releasing the ZnO electrons back into the ZnO conduction band. This increase in the number of shallow donors in the conduction band leads to enhanced photoconductivity of the sample [30].

Figure 3 shows the R and D^* of the PDs versus ± 6 V bias voltage at different solar illumination intensities (25, 50, 75, and 100 mW/cm^2). The D^* depends on the synergism of R and I_{dark} of the devices. Thus, the variation of R and I_{dark} with the bias will intensively influence the relationship of D^* and bias voltage [31]. As seen in Fig. 3, ZnO NRs with different molarities and growth times played an important role in PD performance. High values of R and D^* were shown under high bias voltage, indicating that the PDs were photosensitive to the high bias voltage. It was observed that it started to become more stable from ∼ 1 V. The values of R and D^* decreased the increase in the solar illumination intensity. However, the surface and defect states on ZnO NRs increased the recombination rate and decreased the average lifetime of the carriers under thermal excitation, resulting in the decreased responsivity and detectivity of the devices with the increase in the light intensity [32]. Additionally, the D^* of the PD_{203} and PD_{204} in all PDs tended to decrease which deteriorated the photoresponse

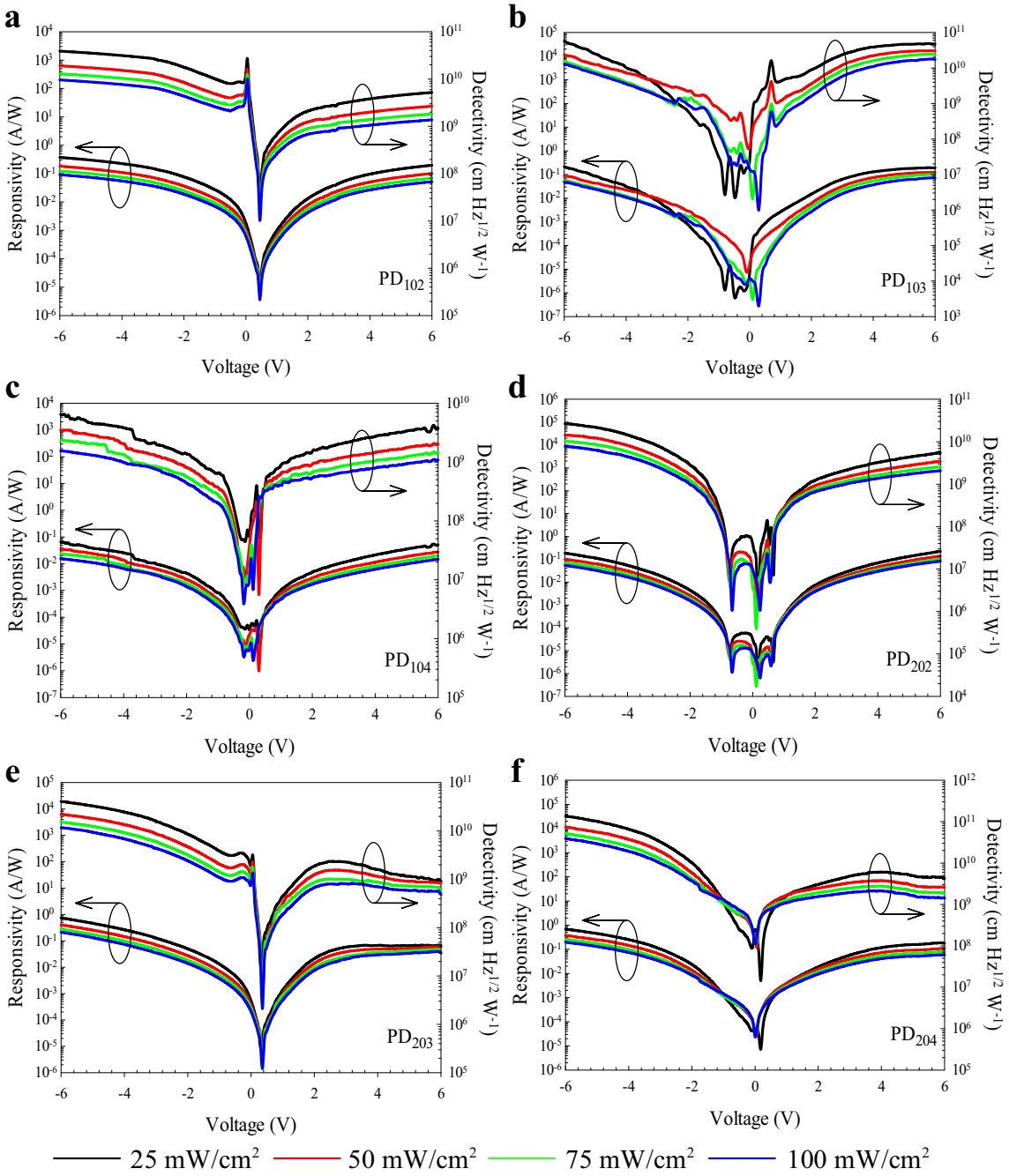

Fig. 3 The responsivity and detectivity of **a** PD_{102}, **b** PD_{103}, **c** PD_{104}, **d** PD_{202}, **e** PD_{203}, and **f** PD_{204} as a function of bias voltage at different solar light intensities

performance at higher bias voltage. At higher bias voltage, the photogenerated charge carriers were not effectively separated due to the presence of trap states in the PD, leading to a decrease in the D^* of PD_{203} and PD_{204}. Due to its high crystalline nature, other PDs were not observed [33]. The values of R and D^* of PDs were found to be 10^{-2}–10^{-1} AW^{-1} and 10^9–10^{11} $cmHz^{1/2}$ W^{-1}, respectively.

4 Conclusions

ZnO NRs were successfully grown on *n*-ZnO/*p*-Si by hydrothermal process. The SEM images showed that the diameter of ZnO NRs was in the range of 62–119 nm. The photoresponse characteristics of ZnO NRs-based PDs were investigated under solar illumination intensity (50 and 100 mW/mm^2) and forward bias voltage (1, 5, and 10 V). It was observed that the fabricated PDs at 90 °C with different molarities (10 and 20 mM) and growth times (2, 3, and 4 h) affected the τ_r, τ_d, S, R, and D^* parameters. The PD_{102} and PD_{103} reached the photocurrent saturation level at 1 V, 5 V, and 10 V, while other PDs reached at 5 V and 10 V under 50 mW/cm^2. Except for PD_{102} and PD_{103}, they were observed to reach saturation levels at 5 V and 10 V under 100 mW/cm^2. Compared to each other, the τ_r and τ_d of the PD_{102} ranged from 58–60 ms to 77–88 ms, respectively. The τ_r and τ_d of the PD_{103} were 66–79 and 63–77 ms, respectively. The S for the PD_{102} ranged from 4.24 to 11.8, while it was in the range of 0.41–7.33 for the PD_{103}. The R was 5.81 AW^{-1} in PD_{102} and 1.19 AW^{-1} in PD_{103}. The D^* was 10^9–10^{11} cmHz$^{1/2}$/W in PD_{102} and 10^{10}–10^{11} cmHz$^{1/2}$/W in PD_{103} at ± 6 V. Considering all these results, the PD_{102} and PD_{103} showed the best performance due to low τ_r and τ_d and high S, R, and D^*.

Acknowledgements

This research was supported by Kastamonu University Scientific Research Projects Coordination Department under the Grant Nos. KU-BAP01/2019-36 and KU-BAP01/2018-106.

Author contributions

All of the authors contributed to the idea, experimental of the research, the analysis of the results, and the writing of the manuscript.

Funding

This research was supported by Kastamonu Üniversitesi [Grant Nos. KU-BAP01/2019-36, KU-BAP01/2018-106].

Data availability

The datasets generated during and/or analyzed during the current study are available from the corresponding author on reasonable request.

Declarations

Conflict of interest All authors declare no conflict of interest regarding this paper.

References

1. O. Çiçek, S. Kurnaz, A. Bekar, Ö. Öztürk, Compos. B **174**, 106987 (2019)
2. N.H. Al-Hardan, A. Jalar, M.A. Abdul Hamid, L.K. Keng, N.M. Ahmed, R. Shamsudin, Sens. Actuators A **207**, 61–66 (2014)
3. S. Singh, Y. Kumar, H. Kumar, S. Vyas, C. Periasamy, P. Chakrabarti, S. Jit, S.-H. Park, Nanomater. Nanotechnol. **7**, 184798041770214 (2017)
4. S. Dhara, K.P. Giri, *Nanorods* (InTech, London, 2012), pp. 1–33
5. M.S. Kumar, D. Chhikara, K.M.K. Srivatsa, Mater. Lett. **65**, 1938–1940 (2011)
6. H. Yang, J. Li, D. Yu, L. Li, Cryst. Growth Des. **16**, 4831–4838 (2016)
7. H.S. Al-Salman, M.J. Abdullah, Measurement **59**, 248–257 (2015)
8. B. Cook, Q. Liu, J. Liu, M. Gong, D. Ewing, M. Casper, A. Stramel, J. Wu, J. Mater. Chem. C **5**, 10087–10093 (2017)
9. C. Soci, A. Zhang, B. Xiang, S.A. Dayeh, D.P.R. Aplin, J. Park, X.Y. Bao, Y.H. Lo, D. Wang, Nano Lett. **7**, 1003–1009 (2007)
10. W. Khan, S.D. Kim, Mater. Sci. Semicond. Process. **66**, 232–240 (2017)
11. K. Liu, M. Sakurai, M. Aono, Sensors **10**, 8604–8634 (2010)
12. L. Luo, Y. Zhang, S.S. Mao, L. Lin, Sens. Actuators A **127**, 201–206 (2006)
13. H.-L. Lu, Y.-Z. Gu, Y. Zhang, X.-Y. Liu, P.-F. Wang, Q.-Q. Sun, S.J. Din, D.W. Zhang, Opt. Express **22**, 22184 (2014)
14. J.P. Kar, S.N. Das, J.H. Choi, T.I. Lee, J. Seo, T. Lee, J.M. Myoung, Appl. Surf. Sci. **257**, 4973–4977 (2011)
15. A.F. Abdurrahman, J. Mater. Sci.: Mater. Electron. **31**, 14357–14374 (2020)
16. M.M.H. Farooqi, R.K. Srivastava, Proc. Natl. Acad. Sci. India Sect. A: Phys. Sci. **90**, 845–859 (2020)
17. H. Huang, G. Fang, X. Mo, L. Yuan, H. Zhou, M. Wang, X. Zhao, Appl. Phys. Lett. **94**, 063512 (2009)

18. Z. Yuan, H. Wu, W. Wang, F. Nie, J. He, J. Nanopart. Res. **22**, 324 (2020)
19. Y. Xie, M. Madel, Y. Li, W. Jie, B. Neuschl, M. Feneberg, K. Thonke, J. Appl. Phys. **112**, 123111 (2012)
20. F.H. Alsultany, Z. Hassan, N.M. Ahmed, Opt. Mater. **60**, 30–37 (2016)
21. S. Ghosh, A. Varghese, K. Thakar, S. Dhara, S. Lodha, Nat. Commun. **12**, 336 (2021)
22. J. Szafraniec, S. Tsao, W. Zhang, H. Lim, M. Taguchi, A.A. Quivy, B. Movaghar, M. Razeghi, Appl. Phys. Lett. **88**, 121102 (2006)
23. R. Khokhra, B. Bharti, H.-N. Lee, R. Kumar, Sci. Rep. **7**, 15032 (2017)
24. Z. Xu, Y. Zhang, Z. Wang, J. Phys. D **52**, 22300 (2019)
25. Z. Guo, D. Zhao, Y. Liu, D. Shen, J. Zhang, B. Li, Appl. Phys. Lett. **93**, 163501 (2008)
26. N.H. Al-Hardan, M.A.A. Hamid, N.M. Ahmed, R. Shamsudin, N.K. Othman, Sens. Actuators A **242**, 50–57 (2016)
27. H.-D. Um, S.A. Moiz, K.-T. Park, J.-Y. Jung, S.-W. Jee, C.H. Ahn, D.C. Kim, H.K. Cho, D.-W. Kim, J.-H. Lee, Appl. Phys. Lett. **98**, 033102 (2011)
28. H.-Y. Chen, K.-W. Liu, X. Chen, Z.-Z. Zhang, M.-M. Fan, M.-M. Jiang, X.-H. Xie, H.-F. Zhao, D.-Z. Shen, J. Mater. Chem. C **2**, 9689–9694 (2014)
29. S. Lany, A. Zunger, Phys. Rev. B **72**, 035215 (2005)
30. B.K. Barnes, K.S. Das, Sci. Rep. **8**, 2184 (2018)
31. P. Tian, L. Tang, J. Xiang, Z. Sun, R. Ji, S.K. Lai, S.P. Lau, J. Konh, J. Zhao, C. Yang, Y. Li, RSC Adv. **6**, 45166–45171 (2016)
32. C. Wei, J.P. Xu, S. Shi, R. Cao, J. Chen, H. Dong, X. Zhang, S. Yin, L. Li, J. Mater. Chem. C **7**, 9769 (2019)
33. B. Roul, R. Pant, S. Chirakkara, G. Chandan, K.K. Nanda, S.B. Krupanidhi, IEEE Trans. Electron Devices **64**, 4161–4166 (2017)